



**HAL**  
open science

## Effects of Co doping on the structure and physicochemical properties of hausmannite ( $Mn_3O_4$ ) and its transformation during aging

Shuang Zhang, Hui Li, Zhongkuan Wu, Jeffrey E. Post, Bruno Lanson, Evert J. Elzinga, Yurong Liu, Haigang Li, Mei Hong, Fan Liu, et al.

### ► To cite this version:

Shuang Zhang, Hui Li, Zhongkuan Wu, Jeffrey E. Post, Bruno Lanson, et al.. Effects of Co doping on the structure and physicochemical properties of hausmannite ( $Mn_3O_4$ ) and its transformation during aging. *Chemical Geology*, 2021, 582, pp.120448. 10.1016/j.chemgeo.2021.120448 . insu-03411470

**HAL Id: insu-03411470**

**<https://insu.hal.science/insu-03411470>**

Submitted on 3 Nov 2021

**HAL** is a multi-disciplinary open access archive for the deposit and dissemination of scientific research documents, whether they are published or not. The documents may come from teaching and research institutions in France or abroad, or from public or private research centers.

L'archive ouverte pluridisciplinaire **HAL**, est destinée au dépôt et à la diffusion de documents scientifiques de niveau recherche, publiés ou non, émanant des établissements d'enseignement et de recherche français ou étrangers, des laboratoires publics ou privés.

1     Effects of Co doping on the structure and physicochemical properties of  
2             hausmannite (Mn<sub>3</sub>O<sub>4</sub>) and its transformation during aging

3     Shuang Zhang<sup>a,b</sup>, Hui Li<sup>c</sup>, Zhongkuan Wu<sup>d</sup>, Jeffrey E. Post<sup>e</sup>, Bruno Lanson<sup>f</sup>, Evert J. Elzinga<sup>g</sup>,  
4     Yurong Liu<sup>a,b</sup>, Haigang Li<sup>h</sup>, Mei Hong<sup>h</sup>, Fan Liu<sup>a,b</sup>, Hui Yin<sup>a,b,\*</sup>

5     <sup>a</sup>Key Laboratory of Arable Land Conservation (Middle and Lower Reaches of Yangtse River),  
6     Ministry of Agriculture and Rural affairs, College of Resources and Environment, Huazhong  
7     Agricultural University, Wuhan 430070, China.

8     <sup>b</sup>State Environmental Protection Key Laboratory of Soil Health and Green Remediation, Ministry  
9     of Ecology and Environment, Huazhong Agricultural University, Wuhan 430070, China.

10    <sup>c</sup>Environmental Sciences Division, Oak Ridge National Laboratory, Oak Ridge, TN 37831

11    <sup>d</sup>College of Environment, Zhejiang University of Technology, Hangzhou 310014, China

12    <sup>e</sup>Department of Mineral Sciences, NHB 119, Smithsonian Institution, Washington DC 20013-7012,  
13    USA

14    <sup>f</sup>Univ. Grenoble Alpes, Univ. Savoie Mont Blanc, CNRS, IRD, Univ. Gustave Eiffel, ISTERre, F-  
15    38000 Grenoble, France

16    <sup>g</sup>Department of Earth and Environmental Sciences, Rutgers University, Newark, NJ 07102, United  
17    States

18    <sup>h</sup>College of Grassland, Resources and Environment, Inner Mongolia Agricultural University,  
19    Hohhot 010018, China

20

21    Corresponding Authors:

22    Tel.: +86 27 87280271. Fax: +86 27 87288618.

23    Email: [yinhui666@mail.hzau.edu.cn](mailto:yinhui666@mail.hzau.edu.cn).

24

25

26 **Abstract:** Hausmannite is a common low-valence manganese oxide mineral with a  
27 distorted spinel structure in surficial sediments. Although natural Mn oxides often  
28 contain various transition metal (TM) impurities, few studies have addressed the  
29 substitution mechanisms of TMs, such as cobalt (Co), with hausmannite and induced  
30 changes in the mineral physicochemical properties. In this study, Co-doped  
31 hausmannites with final Co/Mn molar ratios of 0.05 and 0.11 were synthesized and  
32 characterized by wet chemical analysis, powder X-ray diffraction (XRD), Fourier  
33 transformed infrared spectra (FTIR), high resolution transmission electron microscope  
34 (HRTEM), X-ray photoelectron spectroscopy (XPS) and X-ray absorption fine  
35 structure spectroscopy (XAFS). Co-doped samples have larger crystallite sizes and  
36 smaller specific surface areas than those of the hausmannite without Co. The Co cations  
37 exist in a mixed-valence of +3 and +2. Powder XRD and acid dissolution experiments  
38 indicate that Co incorporates into the mineral structures, and increases the mineral  
39 structural stability. Co K-edge extended X-ray adsorption fine structure (EXAFS)  
40 analysis demonstrates that Co likely substitutes for lattice Mn(III). After aging at room  
41 temperature for three years,  $14.1 \pm 1.9\%$  of pure hausmannite is transformed to  
42 manganite while only  $2.6 \pm 0.7\%$  of manganite appears in the aged Co-doped sample  
43 with an initial Co/Mn molar ratio of 0.10. These results provide new insights into the  
44 incorporation mechanisms of TMs into low valence Mn oxides, and the stability of  
45 these minerals in natural environments.

46 **Keywords:** Mn oxide, hausmannite, transition metal, cobalt, transformation.

47

48

## 49 **1. Introduction**

50 Manganese (Mn) oxide minerals in various geological settings are often enriched  
51 in various transition metals (TMs). Incorporation of TMs into Mn oxides can modify  
52 the mineral substructure, physicochemical properties and reactivity towards various  
53 pollutants (Song et al., 2020; Yin et al., 2012). Our previous studies on the effects of  
54 TMs on the reactivity of hexagonal birnessite towards various pollutants convincingly  
55 demonstrate that the reactivity of these TM-containing minerals, which are close to  
56 natural analogs, can be much different from those of the pure one. For example,  
57 incorporation of Ni into hexagonal birnessite greatly reduces the adsorption densities  
58 of heavy metals,  $Pb^{2+}$  or  $Zn^{2+}$ , on the minerals by 79-85% (Yin et al., 2012). The  
59 removal efficiencies of  $Cr^{3+}$  from water by Co- and Ni-containing birnessites are 28-  
60 55% and 67-78%, respectively, that of the pure birnessite (Yin et al., 2020a).

61 Hausmannite is not only the fifth most common Mn oxide mineral in soils and  
62 sediments, but is also found in hydrothermal and metamorphic deposits (Chartier et al.,  
63 1999; Giovannelli et al., 2012; Jarosch, 1987). It has a tetragonally deformed spinel  
64 structure, elongated along the *c* axis, with  $Mn^{2+}$  occupying the tetrahedral sites and  
65 Jahn-Teller active  $Mn^{3+}$  in the octahedral sites (Bordeneuve et al., 2010; Jarosch, 1987;  
66 Sukhdev et al., 2020). Hausmannite is usually not only the precursor or secondary  
67 product of other Mn oxide phases (Barreto et al., 2020; Birkner and Navrotsky, 2012;  
68 Birkner and Navrotsky, 2014; Feng et al., 2004), but also can have adsorption and redox  
69 reactivity towards a variety of metal pollutants (Barreto et al., 2020; Johnson et al.,  
70 2018; Shaughnessy et al., 2003; Song et al., 2020; Wilk et al., 2005).

71 Being the most widely distributed Mn oxide spinel, hausmannite is capable of  
72 housing various substituents, including Co, Ni, Fe and Al (Antao et al., 2019; Baron et  
73 al., 1998; Bordeneuve et al., 2010; Green et al., 2004; Lefkowitz and Elzinga, 2015;  
74 Rajeesh Kumar et al., 2021; Song et al., 2020). Substitution of  $Fe^{3+}$  for  $Mn^{3+}$  into the  
75 octahedral site in hausmannite decreases the Jahn-Teller distortion, increases the Curie  
76 point, and decreases the spontaneous magnetization (Baron et al., 1998). Zn doping  
77 changes the morphologies of the obtained hausmannite crystallites from nanorods for  
78 the pure mineral to a mixture of nanorods and nanoparticles, and increases the energy

79 bandgap (Jha et al., 2012). Pb doping greatly reduces the  $Mn_3O_4$  particle size and  
80 increases the bandgap, dielectric constant, and AC conductivity (Şahin et al., 2020).  
81 Doping with various TMs ( $Cr^{3+}$ ,  $Co^{2+}$ ,  $Ni^{2+}$ , and  $Cu^{2+}$ ) greatly enhances the phase  
82 stability during cycling and charge-transfer behaviors of hausmannite (Dong et al.,  
83 2013). However, these studies mainly focus on the applications of TM-modified  
84 hausmannites in materials sciences. It is recently reported that Ni substitution in  
85 hausmannite causes noticeable changes in the mineral structure (e.g. lattice parameters),  
86 and enhances mineral acid dissolution and oxidation reactivity towards As(III) at pH =  
87 5 (Song et al., 2020). This indicates that structural impurities may modify the structure  
88 and physicochemical properties of hausmannite and thus the adsorption and redox  
89 reactivity towards pollutants. Unlike Ni, Co is highly redox-sensitive, and the influence  
90 of Co incorporation on the reactivity and stability of hausmannite remains to be  
91 determined.

92 Further, as a kind of metastable mineral, hausmannite can be converted into other  
93 Mn oxides phases during aging. These processes can be affected by mineral properties,  
94 such as chemical composition and particle sizes, and environmental conditions, e.g.,  
95 moisture, temperature and  $O_2$  (Birkner and Navrotsky, 2012; Birkner and Navrotsky,  
96 2014; Kirillov et al., 2009; Rabiei et al., 2005). At 60% relative humidity at room  
97 temperature, hausmannite can change its morphology and chemical identity to  
98 manganite (Rabiei et al., 2005). Upon slow oxidation at room temperature for 1 year,  
99 the hausmannite content in a mixture of hausmannite with manganite is decreased from  
100 47% to 28% (Kirillov et al., 2009). Small crystallite size is reported to promote  
101 hausmannite transformation (Birkner and Navrotsky, 2012; Birkner and Navrotsky,  
102 2014). These previous studies mainly focus on the aging of pure hausmannite. However,  
103 the effect of TM doping on the stability of hausmannite and its transformation during  
104 aging remains largely unexplored.

105 The present work aims to investigate the effect of Co doping on the mineral  
106 structure, physicochemical properties and stability during aging at room temperature.  
107 Specifically, Co-doped hausmannite samples were synthesized at room temperature by  
108 a coprecipitation method, and characterized by powder XRD, FTIR and HRTEM. The

109 valence and crystal chemistry of Mn and Co were investigated by XPS, Co K-edge  
110 XAFS and acid dissolution experiments. These findings will help in understanding the  
111 effects of TM doping on the structure, properties and stability of low valence Mn oxide  
112 minerals in natural environments.

113

## 114 **2. Materials and methods**

### 115 **2.1 Preparation of Co-doped hausmannites**

116 Cobalt substituted hausmannite was prepared according to the method described  
117 in Giovannelli (Giovannelli et al., 2012). In detail,  $\text{CoSO}_4 \cdot 7\text{H}_2\text{O}$  was added to 200 mL  
118 of 0.5 M  $\text{MnSO}_4$  solution to obtain an initial Co/Mn molar ratio of 0, 0.05 and 0.10.  
119 After the solution was uniformly mixed, 2 M NaOH solution was added dropwise to  
120 keep the suspension pH above 10 for 6 h under stirring in air at room temperature. The  
121 pH was recorded by a pH-meter. At the end of the reaction, the slurry was filtered,  
122 rinsed with deionized water until the conductivity of filtrate was  $< 20 \mu\text{s cm}^{-1}$  to  
123 eliminate the salt excess, and dried at 40 °C for 3 days, and then ground and sieved (100  
124 mesh). The prepared samples were designated as HM, CoH5, and CoH10  
125 correspondingly.

126 Portions of the HM and CoH10 powders were stored in closed tubes at room  
127 temperature ( $25 \pm 5$  °C) under air condition in the laboratory for three years, and the  
128 humidity in laboratory around 50%. The corresponding samples were named as  
129 agedHM and agedCoH10.

### 130 **2.2 Sample characterization**

131 The phase purity of prepared samples was analyzed using a Bruker D8 Advance  
132 diffractometer with Cu  $K\alpha$  radiation ( $\lambda = 0.15418$  nm). The diffractometer was operated  
133 at a tube voltage of 40 kV and a tube current of 40 mA in the range of  $2\theta$  of 5-85 ° at a  
134 step of 0.02 ° and an integration time of 1.2 s. Rietveld structure refinements were  
135 performed using software TOPAS (version 4.2). The specific surface areas (SSA) were  
136 measured by  $\text{N}_2$  adsorption at liquid nitrogen temperature (77 K) with an Autosorb-1  
137 standard physical adsorption analyzer (Quantachrome Autosorb-1, USA). The samples  
138 (100 mg) were degassed under vacuum at 110 °C for 3 h before  $\text{N}_2$  adsorption, and SSA

139 was calculated by employing the multi-point BET method. HRTEM analysis and  
140 selected-area electron diffraction were employed to obtain mineral morphologies,  
141 particle sizes, and phase lattice on a JEM-2100F (JEOL, Japan) at 200 keV. The samples  
142 were prepared by adding 50  $\mu\text{L}$  of 0.1  $\text{g}\cdot\text{L}^{-1}$  mineral suspension onto a 200-mesh  
143 carbon-coated copper grid (Beijing Zhongjingkeyi Technology Co., Ltd.), and dried at  
144 room temperature under air condition. FTIR analyses were performed on a Bruker  
145 Equinox 55 model spectrophotometer using KBr pellets with a spectral range of 4000-  
146 400  $\text{cm}^{-1}$ . XPS of Mn 2p and Co 2p were measured on a VG Multilab 2000 X-ray  
147 photoelectron spectrometer with a Mg  $\text{K}\alpha$  X-ray source (1253.6 eV) using the large  
148 area mode with a pass energy of 25 eV and an energy step size of 0.1 eV. Adventitious  
149 C 1s binding energy was used to calibrate the energy and set to 284.8 eV. Data were  
150 analyzed using Avantage software, and a Shirley background was used (Yin et al., 2011).  
151 For Mn 2p fitting, the fit parameters were used from a previous study (Ilton et al., 2016).

152 The sample chemical composition was determined via atomic absorption  
153 spectrometry (AAS, Varian AAS 240FS) after dissolving 0.1000 g solid in a mixture of  
154 25 mL of 0.25 M  $\text{NH}_2\text{OH}\cdot\text{HCl}$  solution and 1 M  $\text{H}_2\text{SO}_4$  solution. Triplicate analyses  
155 were performed. Method blanks and matrix spikes were also analyzed along with  
156 samples for quality assurance and quality controls, and the spiked recoveries of  $\text{Mn}^{2+}$   
157 were between 98 and 102% (mean recovery:  $100 \pm 2\%$ ).

### 158 **2.3 Dissolution experiments**

159 The acid dissolution experiment was performed by adopting the method in our  
160 previous study (Qin et al., 2017). Briefly, 0.10 g sample was added into 250 mL of 2 M  
161 HCl solution while stirring at a constant rate with a magnetic stir at room temperature.  
162 At predetermined time intervals, an aliquot of 5 mL suspension was taken out and  
163 immediately filtered through 0.22  $\mu\text{m}$  membrane (Shanghai Xingya purification  
164 material factory). The concentration of  $\text{Mn}^{2+}$  and  $\text{Co}^{2+}$  in the filtrate were analyzed using  
165 AAS. The metal (Me) dissolution ratio was calculated as  $\chi_{\text{Me}} = \text{Me}(t)/\text{Me}(\text{total})$ , where  
166 Me (t) is the concentration of metal in solutions at time t, and Me(total) is the final metal  
167 concentration after complete dissolution of the mineral.

### 168 **2.4 X-ray absorption fine structure (XAFS) spectroscopy**

169 The XAFS data were collected at room temperature on the 1W1B beamline at the  
170 Beijing Synchrotron Radiation Facility (BSRF) (Yin et al., 2012). Cobalt K-edge XAFS  
171 data were collected in fluorescence mode over the energy range of 7510 to 8305 eV.  
172 Reduction and analysis of XAFS data were performed using Athena and Artemis from  
173 the IFEFFIT software package (Ravel and Newville, 2006). Cobalt K-edge spectra were  
174 background-subtracted using the following parameters:  $E_0 = 7716$  eV,  $R_{bkg} = 1.0$  Å  
175 and  $k\text{-weight} = 2$ . Structural parameters (bond length (R), coordination number (CN),  
176 and Debye-Waller factor ( $\sigma^2$ )) were obtained by fitting the  $k^3$ -weighted EXAFS data to  
177 the standard EXAFS equation (Kelly et al., 2008). Phase and amplitude functions were  
178 calculated using FEFF7.0 (Rehr et al., 1992). The Co K-edge EXAFS data were fitted  
179 in an R space of 1-4 Å over a k range of 3.1-12.0 Å<sup>-1</sup>, using several single scattering  
180 paths calculated by substituting Co for tetrahedral or octahedral Mn in the hausmannite  
181 structure (ICSD 76088). An amplitude reduction factor ( $S_0^2$ ) of 0.877 for Co was  
182 adopted from our previous studies (Yin et al., 2014). In all fits, the number of  
183 independent variables was much smaller than that of the independent data points  
184 allowed. During Fourier transformation and EXAFS data fitting, a Hanning window  
185 was used.

186

## 187 **3 Results**

### 188 **3.1 Powder XRD**

189 Three synthesized samples display similar XRD patterns (Fig. 1a), which coincide  
190 well with the tetragonal hausmannite standard (ICDD 89-4837). The main characteristic  
191 reflections at  $\sim 3.10$  Å,  $\sim 2.77$  Å,  $\sim 2.49$  Å,  $\sim 1.58$  Å, and  $\sim 1.54$  Å can be indexed to (112),  
192 (103), (211), (321), and (224), respectively (Giovannelli et al., 2012; Zhao et al., 2011).  
193 With an increase in Co content, the peak positions of the ( $hk0$ ) reflections do not change  
194 but those of ( $hkl$ ) reflections shift to higher angles, indicating a decrease of unit-cell  
195 parameter  $c$ . Rietveld refinements of these samples were performed using the  
196 hausmannite structure (ICSD 76088) as the starting model. Because of the similarity of  
197 the Co and Mn X-ray scattering factors, the refinements were not able to provide  
198 information about ordering of the Co cations over the tetrahedral and octahedral sites

199 or the Co valence. The refinements were thus carried out assuming all Mn, and the  
200 results are listed in Fig. 1a and Table S1. From HM to CoH10, unit-cell parameter  $a$  is  
201 essentially constant at 5.771-5.774 Å, while parameter  $c$  systematically decreases from  
202  $9.477 \pm 0.002$  Å to  $9.370 \pm 0.002$  Å. The indicator of Jahn-Teller distortion of the  
203  $[\text{Mn(III)O}_6]$  octahedron in hausmannite,  $c/(1.414a)$ , likewise decreases from  $1.1613 \pm$   
204  $0.0003$  for HM to  $1.1479 \pm 0.0004$  for CoH10, indicating the reduction of Jahn-Teller  
205 distortion after Co doping (Bordeneuve et al., 2010; Hirai et al., 2016; Kim et al., 2012).  
206 In hausmannite, the  $[\text{Mn(III)O}_6]$  octahedra are elongated along the  $[001]$  direction  
207 (Jarosch, 1987), therefore the decrease in  $c$  and the Jahn-Teller distortion indicator  
208 clearly confirm the replacement of lattice  $\text{Mn}^{3+}$  by the smaller  $\text{Co}^{2+/3+}$  and/or  $\text{Mn}^{4+}$   
209 (Bordeneuve et al., 2010; Hirai et al., 2016; Shannon, 1976; Song et al., 2020). The  
210 coherent scattering domain (CSD) sizes determined by the refinements for HM, CoH5  
211 and CoH10 are  $59.1 \pm 0.7$  nm,  $91.6 \pm 1.1$  nm and  $74.9 \pm 1.3$  nm, respectively. This may  
212 suggest that Co doping promotes the hausmannite crystal growth at the experimental  
213 conditions.

214 The powder XRD analysis of three years aged HM (agedHM) and CoH10  
215 (agedCoH10) is plotted in Fig. 1b. In addition to the main reflections of hausmannite  
216 (ICSD 76088), there is an additional peak at  $2\theta$  of  $26.18^\circ$  in agedHM. This peak  
217 coincides well with that of manganite (ICSD 84949). This peak also appears in  
218 agedCoH10, but with much lower intensity than that in agedHM. This suggests that Co-  
219 doped hausmannite sample undergoes slower oxidation at room temperature during  
220 aging in the dry state than that of pure hausmannite. Quantitative phase analysis of these  
221 aged samples were performed using the hausmannite (ICSD 76088) and manganite  
222 structure (ICSD 84949). The results are depicted in Fig. 1b and Table S2. For agedHM,  
223 the contents of hausmannite and manganite are  $85.9 \pm 1.9\%$ , and  $14.1 \pm 1.9\%$ ,  
224 respectively. For agedCoH10, the contents of hausmannite and manganite are  $97.4 \pm$   
225  $0.7\%$  and  $2.6 \pm 0.7\%$ , respectively.

### 226 3.2 Elemental analysis, specific surface areas and morphologies

227 With increasing Co content, the Mn content decreases from  $70.92 \pm 0.01\%$  for HM  
228 to  $69.63 \pm 0.32\%$  and  $65.93 \pm 1.16\%$  for CoH5 and CoH10, respectively. The final

229 Co/Mn molar ratios in these samples are approximately the same as those in the initial  
230 reactants. The specific surface area (SSA) of HM is  $12.4 \text{ m}^2 \cdot \text{g}^{-1}$ , and decreases to  $11.7$   
231  $\text{m}^2 \cdot \text{g}^{-1}$  and  $11.8 \text{ m}^2 \cdot \text{g}^{-1}$  for CoH5 and CoH10, respectively.

232 Fresh HM crystals are composed of irregular cubic particles (Fig. 2a), which is  
233 consistent with previous studies (Giovannelli et al., 2012; Hao et al., 2011; Zhang et al.,  
234 2011). Co-doped hausmannite crystals are uniformly composed of cubic particles (Fig.  
235 2b, c), which are also similar to Co-doped hausmannite samples in previous studies  
236 (Dong et al., 2013). Statistical analysis of the particle sizes of these samples gives an  
237 average size of  $85 \pm 18 \text{ nm}$  of HM,  $131 \pm 27 \text{ nm}$  of CoH5 and  $103 \pm 28 \text{ nm}$  of CoH10  
238 (Fig. S1). These physical sizes coincide well with the CSD sizes obtained by powder  
239 XRD analysis. Both suggest that Co-doped samples have larger sizes than the pure one.  
240 This may indicate that Co ions play a significant role in the growth and assembly of  
241 hausmannite initial crystals, and a low amount of Co may favor the crystal growth of  
242 hausmannite; but further increasing the Co content will cause structural defects in the  
243 mineral structure and thus retard the crystal growth.

244 In order to confirm whether these Co-doped hausmannite samples are stable during  
245 dry storage at room temperature, the HRTEM and SAED patterns of the samples  
246 obtained after aging for 3 years, agedHM and agedCoH10, are also presented in Fig.  
247 2d-i. There are plenty of lath-like crystals in agedHM, besides the cubic crystals (Fig.  
248 2d). The SAED pattern of the cubic crystal (Fig. 2e) confirms that the cubes are pure  
249 hausmannite single crystals. In the HRTEM image of the lath crystal (Fig. 2f), a lattice  
250 distance of  $0.339 \text{ nm}$  is observed, matching well with that of manganite. The crystals  
251 of agedCoH10 retain their cubic shapes for hausmannite (Fig. 2g), which is also  
252 confirmed by HRTEM and SAED (Fig. 2h, i).

### 253 3.3 FTIR

254 The FTIR spectra of these freshly prepared Co-doped hausmannite samples have  
255 four peaks located at  $408$ ,  $525$ ,  $629$ , and  $3415 \text{ cm}^{-1}$  (Fig. 3). These bands coincide well  
256 with those of hausmannite (Kirillov et al., 2009). The  $3415 \text{ cm}^{-1}$  band is assigned to OH  
257 vibrations of physisorbed water molecules, while the three other peaks from left to right  
258 correspond to wagging, bending and stretching vibrations of  $[\text{MnO}_6]$  and  $[\text{MnO}_4]$  units

259 (Julien et al., 2004; Kirillov et al., 2009).

260 After three years aging in the dry state, the spectra of these hausmannites change.  
261 Firstly, a peak at  $1630\text{ cm}^{-1}$  appears (Fig. 3). As this peak corresponds to molecular  $\text{H}_2\text{O}$   
262 bending vibrations (Kim et al., 2002), the presence of this peak suggests there is a  
263 quantity of physisorbed water on the mineral surfaces and/or in the structures. Secondly,  
264 although the main peaks for hausmannite are preserved in the spectrum of agedHM, the  
265 relative intensities of the peaks belonging to manganite, such as 440, 484, 597, 1085,  
266 1116, 1152, 2075 and  $2655\text{ cm}^{-1}$  have increased. This indicates a significant portion of  
267 hausmannite is transformed into manganite during the aging (Kirillov et al., 2009;  
268 Kohler et al., 1997). Additionally, careful inspection of the spectrum of agedCoH10  
269 shows that, the original  $525\text{ cm}^{-1}$  peak of fresh CoH10 is shifted to  $508\text{ cm}^{-1}$  for  
270 agedCoH10, and there are three small additional peaks at 1085, 1116 and  $1152\text{ cm}^{-1}$ ,  
271 indicating the presence of a minor amount of manganite (Fig. 3e-h). This agrees well  
272 with the XRD analysis. Additionally, the bands for agedHM and agedCoH10 are weaker  
273 and broader relative to the initial samples, owing to the coexistence of several Mn oxide  
274 phases.

### 275 3.4 Mn 2p XPS spectra

276 Manganese 2p spectra of these samples are used to investigate the proportions of  
277 various Mn species on the mineral surfaces. With Co content increasing, the peak  
278 binding energy (BE) shifts to low BE side (Fig. 4a). For example, the Mn  $2p_{3/2}$  BE is  
279 decreased from 641.94 eV for HM to 641.01 eV for CoH10, indicating the decrease of  
280 the Mn average oxidation state (AOS). Further quantitative fitting analysis of the  
281 spectrum using multiplet parameters (Ilton et al., 2016) are conducted (Fig. 4b, c and  
282 Table S3). The HM spectrum can be decomposed to 28%  $\text{Mn}^{2+}$ , 58%  $\text{Mn}^{3+}$  and 14%  
283  $\text{Mn}^{4+}$ . With the increase of the dopant level, the relative proportions of  $\text{Mn}^{3+}$  and  $\text{Mn}^{4+}$   
284 are decreased but that of  $\text{Mn}^{2+}$  is increased. The spectrum of CoH10 can be decomposed  
285 to 39%  $\text{Mn}^{2+}$ , 54%  $\text{Mn}^{3+}$  and 7%  $\text{Mn}^{4+}$ . The calculated Mn AOSs are  $2.86 \pm 0.02$  and  
286  $2.69 \pm 0.02$  for HM and CoH10, respectively.

### 287 3.5 Acid dissolution experiments

288 Fig. 5 shows the fraction of dissolved Co or Mn ( $\chi_{\text{Co}}$  or  $\chi_{\text{Mn}}$ ) vs. time, and  $\chi_{\text{Co}} - \chi_{\text{Mn}}$

289 curves of the Co-doped samples in 2 M HCl solution at room temperature. For both  
290 samples, the  $\chi_{\text{Co}}$  or  $\chi_{\text{Mn}}$  vs. time curves show a fast initial rate, followed by a gradual  
291 decrease until the dissolution is complete, and the dissolution of Co is slightly quicker  
292 than that of Mn. To obtain the Mn and Co dissolution rate constant (K), Kabai equation,  
293  $\chi_{\text{Metal}} = 1 - \exp(-(\text{K} \cdot t)^a)$ , is employed to model the dissolution curves (Alvarez et al., 2007;  
294 Liu et al., 2019). With Co content increasing, the Mn dissolution rate constant ( $\text{K}_{\text{Mn}}$ ) is  
295 decreased from  $0.2823 \pm 0.0301 \text{ min}^{-1}$  for CoH5 to  $0.2070 \pm 0.0175 \text{ min}^{-1}$  for CoH10.  
296 These results indicate that doping Co makes the mineral structure more stable and more  
297 resistant to proton attack. This may be related to the higher bond dissociation energy  
298 (BDE) of Co-O ( $397 \pm 9 \text{ kJ} \cdot \text{mol}^{-1}$ ) than that of Mn-O ( $362 \pm 25 \text{ kJ} \cdot \text{mol}^{-1}$ ) (Lide and  
299 “Mickey” Haynes, 2010). According to the BDE, it is expected that Mn cations will be  
300 slightly easier to be released out of the lattice than Co cations. In contrast, the  
301 dissolution-rate constant of Co is much higher than that of Mn, and increases with  
302 increasing the Co content in the sample. The Co dissolution rates ( $\text{K}_{\text{Co}}$ ) in these samples  
303 are  $0.6516 \pm 0.0724 \text{ min}^{-1}$  for CoH5 and  $0.8743 \pm 0.0804 \text{ min}^{-1}$  for CoH10, respectively.  
304 This may suggest that Co may not occupy completely the same lattice sites as Mn. But  
305 it should also be noteworthy that, the mineral dissolution in HCl solution is a much  
306 complex process, which involves protonation, complexation, and reduction induced  
307 dissolutions by  $\text{Cl}^-$  (Cornell and Schwertmann, 2003). It can be affected by many other  
308 factors such as crystal sizes, coexisted cations,  $\text{H}^+$  concentration and so on. Particles  
309 with smaller crystal sizes are dissolved faster than those with large crystal sizes  
310 (Alvarez et al., 2007; Cornell and Schwertmann, 2003). The obtained  $\alpha$  values for  $\chi_{\text{Co}}$ -  
311  $t$  or  $\chi_{\text{Mn}}$ - $t$  for CoH5 and CoH10 are also the same, confirming the purity of these  
312 minerals. Further, the  $\chi_{\text{Co}}$  -  $\chi_{\text{Mn}}$  curves are a little convex with respect to the  $Y=X$  line.  
313 This suggests Co incorporates into the mineral structures but is slightly preferentially  
314 enriched in the rims of the crystals (Qin et al., 2017; Yin et al., 2014).

### 315 **3.6 Co K-edge XAFS analysis**

#### 316 **3.6.1 X-ray adsorption near edge structure (XANES)**

317 The Co K-edge XANES profiles of the two Co-doped hausmannite samples, CoH5

318 and CoH10, are distinct from but intermediate between those of the reference  
319 compounds CoSO<sub>4</sub> and CoOOH (Fig. 4d), suggesting a mixed-valence of Co in these  
320 samples. Linear combination fitting analysis further quantitatively confirms this (Fig.  
321 4d and Table S4). The results show that CoH5 and CoH10 both contain 66-67% Co<sup>3+</sup>  
322 and 33-34% Co<sup>2+</sup>. Previous studies reported that Co exists as only Co<sup>2+</sup> in Co-  
323 containing hausmannite (Mn<sub>3-x</sub>Co<sub>x</sub>O<sub>4</sub>, 0 < x < 1) samples synthesized under mild  
324 alkaline conditions and at high temperature (Bordeneuve et al., 2010; Dong et al., 2013;  
325 Hirai et al., 2016). In contrast, the samples used here were synthesized using a  
326 coprecipitation method at room temperature and at pH > 10.

### 327 3.6.2 EXAFS

328 The k<sup>3</sup>-weighted Co K-edge EXAFS and the corresponding Fourier transformed  
329 spectrum (FT) of typical Co-doped sample, CoH10, are different from those of CoOOH  
330 and CoSO<sub>4</sub> references (Yin et al., 2015), indicating neither CoOOH precipitate nor free  
331 Co<sup>2+</sup> exists (Fig. 6a,b). As both powder XRD analysis and acid dissolution confirm the  
332 incorporation of Co into the mineral structures, Co can exist in either an octahedral or  
333 a tetrahedral coordination or both. The oscillations of CoH5 and CoH10 are essentially  
334 the same (Fig. 6c,d), indicating that Co ions in the two samples have similar  
335 coordination environments. The corresponding FTs show two strong backscattering  
336 neighbors at R + ΔR ~ 1.5 Å and ~ 2.9 Å. The former corresponds to the first Co-O pair,  
337 and the later can be deconvoluted into several Co-Me (Me = Mn and Co) pairs  
338 (Bordeneuve et al., 2010).

339 To obtain more detailed information about the local structures of Co in the Co-  
340 doped hausmannite samples, the Co K-edge EXAFS spectra of CoH5 and CoH10 are  
341 analyzed with shell-by-shell fits (Fig. 6c, d and Table 1). The results indicate an average  
342 Co-O distance of 1.97 ± 0.02 Å, which is slightly longer than those (1.90-1.91 Å)  
343 previously reported for octahedral Co<sup>3+</sup> (Manceau et al., 1997; Yin et al., 2013; Yin et  
344 al., 2015), but much shorter than for octahedral Co<sup>2+</sup> (2.09 Å) (Manceau et al., 1997).  
345 This further suggests the coexistence of Co<sup>3+</sup> and Co<sup>2+</sup> in the hausmannites. Although  
346 cations in tetrahedral coordination, such as Zn<sup>2+</sup>, typically form shorter distances with  
347 the first coordination O (Kwon et al., 2009), the case for Co is complex. It was reported

348 that in YBaCo<sub>4</sub>O<sub>7</sub>, the average tetrahedral Co-O distance ranges from 1.90-1.92 Å  
349 (Valldor and Andersson, 2002). Thus, it is difficult to distinguish octahedral from  
350 tetrahedral Co based on Co-O distances alone. The fits also indicate longer Co-Me  
351 (Me=Co, Mn) correlations at radial distances of 2.80-2.82, 3.01-3.02, 3.36-3.38 and  
352 3.77-3.78 Å (Table 1). These values correspond to the distances between edge-sharing  
353 octahedra in the *a*- and *c*-direction, and corner-sharing octahedron-tetrahedron pairs in  
354 the *a*- and *c*-direction, respectively, matching well with those for Co located in the  
355 octahedron sites (Table S1). Further, when comparing to the corresponding average Me-  
356 Me distances obtained by Rietveld structure refinements (Table S1), these Co-Me  
357 distances are shorter, owing to the smaller radius of Co(III) (Shannon, 1976).

358 EXAFS fittings assuming that all the Co cations occupy the tetrahedral sites are  
359 also conducted. An average Co-O distance of  $1.96 \pm 0.01$  Å is derived, which is almost  
360 the same as that determined assuming all octahedral Co. An attempt to fit the  $R + \Delta R \sim$   
361 2.9 Å peak by combining four paths: two paths for octahedron-tetrahedron corner-  
362 sharing pairs in the *a*- and *c*-axis, a path for the nearest tetrahedron-tetrahedron pairs  
363 and a Co-O path corresponding to that between the center Mn in a tetrahedron and its  
364 second shell O belonging to the corner-sharing octahedron, does not yield a reasonable  
365 fit. This suggests that the vast majority of Co cations occupy the octahedral sites in Co-  
366 doped hausmannites (Song et al., 2020).

367

## 368 4. Discussion

### 369 4.1 Co valence and crystal chemistry in Co-doped hausmannite

370 Cobalt K-edge XANES analysis showed that Co<sup>2+</sup> and Co<sup>3+</sup> coexist in the Co-  
371 doped hausmannites. Interestingly, the Co<sup>3+</sup>/Co<sup>2+</sup> ratios keep almost the same, ~2, for  
372 CoH5 and CoH10. Owing to the high redox potential of Co<sup>3+</sup>/Co<sup>2+</sup> pair ( $E^0 = 1.92$  V)  
373 (Lide and “Mickey” Haynes, 2010), O<sub>2</sub> and high valence Mn in the mineral, and surface  
374 catalytic oxidation may account for the Co<sup>2+</sup> oxidation. The oxidation of Co<sup>2+</sup> is highly  
375 related to the solution conditions, e.g. pH and temperature. Generally, a high  
376 concentration of OH<sup>-</sup> and high temperature favors the oxidation (Alvarez et al., 2008;  
377 Pozas et al., 2004; Yin et al., 2020b). The coexistence of Co<sup>2+</sup> and Co<sup>3+</sup> in the doped

378 hausmannite samples is similar to that observed in Co-doped goethite samples in our  
379 previous study (Yin et al., 2020a), both owing to the low alkalinity and low temperature  
380 used. However, in the Co-doped goethite series, the  $\text{Co}^{3+}/\text{Co}^{2+}$  ratio increases with  
381 increasing initial Co concentration. This is ascribed to the catalytic oxidation of  $\text{Co}^{2+}$   
382 on the mineral precursor (e.g. ferrihydrite) surfaces driven by the electric potential  
383 energy, which is dependent on the redox cation concentration (Boland et al., 2013; Lan  
384 et al., 2017; Yin et al., 2020a). The constant  $\text{Co}^{3+}/\text{Co}^{2+}$  ratio here may possibly be  
385 explained by the absence of surface catalytic oxidation behaviors on hausmannite  
386 surfaces, because hausmannite is an insulator (Bordeneuve et al., 2010).

387 Powder XRD, acid dissolution experiments and Co K-edge EXAFS analysis  
388 demonstrate that the Co cations are incorporated into the mineral structures. In  
389 hausmannite,  $\text{Mn}^{2+}$  occupies the tetrahedral site while  $\text{Mn}^{3+}$  occupies the octahedral  
390 sites. However, when exotic cations are incorporated into the structure, the crystal  
391 chemistry of the exotic cations are complex. Structure analysis of cobalt manganese  
392 oxide spinel ( $\text{Mn}_{3-x}\text{Co}_x\text{O}_4$ ) ( $0 \leq x \leq 3$ ) synthesized at 800 °C demonstrates that the  
393 tetrahedral Mn is first preferentially substituted by Co for  $x < 1$ , and then the octahedral  
394 Mn is replaced by Co with increasing x value. It also shows that  $\text{Mn}^{2+}$  and/or  $\text{Co}^{2+}$  fill  
395 the tetrahedral sites while  $\text{Mn}^{3+}$ ,  $\text{Co}^{2+}$ , low-spin state  $\text{Co}^{3+}$  and  $\text{Mn}^{4+}$  occupy the  
396 octahedral site (Bordeneuve et al., 2010). For a series of  $\text{Mn}_{3-x}\text{Co}_x\text{O}_4$  samples ( $0 \leq x \leq$   
397 1.5) synthesized at ~20 °C by coprecipitation of the mixtures of  $\text{Mn}^{2+}$  and  $\text{Co}^{2+}$  solution  
398 using  $\text{NH}_3 \cdot \text{H}_2\text{O}$ , the  $\text{Mn(III)O}_6$  distortion indicator,  $c/\sqrt{2a}$ , almost overlaps with those  
399 for the samples from the previous study when  $x < 1$ , and Co cations in these samples  
400 was thought to solely occupy the tetrahedral sites (Hirai et al., 2016). Comparison of  
401 the  $c/\sqrt{2a}$  of the Co-doped hausmannite samples in the present study with those from  
402 previous studies indicates that there is a good linear relationship between Co content  
403 and  $c/\sqrt{2a}$  for all these samples when  $x < 1$ , but the dependence of  $c/\sqrt{2a}$  to the sample  
404 Co content varies much. The  $c/\sqrt{2a}$  of our samples decreases much faster with  
405 increasing Co content than that in literatures, with a slope ~ 2 times that of the later  
406 (Fig. 7). This may indicate that the crystal chemistry of Co in our samples is not the  
407 same as that in the previous studies, owing to the fact that the mineral preparation

408 method will affect the detailed crystal chemistry of Co (Zhao et al., 2017).

409 Further, there is a debate in the spin state of the cations in the hausmannite  
410 structure. Some literatures reported that in the distorted spinel structure of hausmannite,  
411  $Mn^{2+}$  is in the low-spin state (LS) while  $Mn^{3+}$  is in the high-spin state (HS) (Bordeneuve  
412 et al., 2010; Jarosch, 1987; Nogués and Poix, 1974). However, other studies adopted  
413 that  $Mn^{3+}$  in hausmannite octahedral sites has a low-spin state while  $Mn^{2+}$  in tetrahedral  
414 sites has a high-spin state (Boucher et al., 1971; Xu et al., 2005). According to  
415 molecular orbital calculations, if the  $MnO_6^{9-}$  cluster has smaller exchange splitting of  
416 the  $2t_{2g}$  orbital and larger crystal field splitting, a transition of Mn(III) from HS to LS  
417 can occur, in company with a decrease of Mn-O distance from 2.04 to 1.88 Å (Sherman,  
418 1984). The average Mn-O distances in  $[Mn(III)O_6]$  in our Co-doped hausmannites are  
419 2.05-2.06 Å (Table S1). This probably suggests that Mn(III) in our hausmannites are  
420 probably HS. In the normal spinel structure of  $Co_3O_4$ , HS  $Co^{2+}$  occupies the tetrahedral  
421 sites while LS  $Co^{3+}$  occupies the octahedral sites (Spencer and Schroerer, 1974). In order  
422 to elucidate the possible distributions of various cations in these Co-doped hausmannite  
423 samples, the basic physicochemical properties of these cations are compared (Table 2).

424 After Co doping, the proportions of  $Mn^{3+}$  and  $Mn^{4+}$  are decreased while that of  
425  $Mn^{2+}$  is increased with increasing dopant content. It is generally assumed that  $Co^{3+}$  in  
426 octahedral sites exists mostly in the LS state (Burns, 1993; McKenzie, 1970; Yin et al.,  
427 2013). The CFSE of LS  $Co^{3+}$  ( $534.2 \text{ kJ}\cdot\text{mol}^{-1}$ ) is  $\sim 2.5$  times larger than that of  $Mn^{3+}$  in  
428 the hausmannite structure, and therefore, it is favorable for  $Co^{3+}$  to replace  $Mn^{3+}$ . This  
429 is the same for LS  $Co^{2+}$ . The CFSE of octahedrally coordinated LS  $Co^{2+}$  ( $198.2 \text{ kJ}\cdot\text{mol}^{-1}$ )  
430 is larger than that of HS  $Mn^{3+}$  in hausmannite, favoring the substitution of  $Mn^{3+}$  by  
431  $Co^{2+}$ . This is supported by the Co K-edge EXAFS analysis. Further, as the radius of LS  
432  $Co^{3+}$  in octahedral coordination is 12.7% smaller than that of HS  $Mn^{3+}$ , this substitution  
433 also accounts for the decrease of unit-cell parameter  $c$  and the suppression of the Jahn-  
434 Teller distortion. Further, the smaller CFSE of tetrahedral HS Co(II) ( $58.7 \text{ kJ}\cdot\text{mol}^{-1}$ )  
435 than that of LS Mn(II) ( $79.6 \text{ kJ}\cdot\text{mol}^{-1}$ ) in tetrahedron excludes the substitution of Co(II)  
436 for tetrahedral Mn(II). Consequently, it is assumed that in the Co-doped hausmannite  
437 samples low-spin  $Co^{2+}$  and  $Co^{3+}$  occupy the octahedral sites.

## 438 4.2 Hausmannite transformation during aging

439 After aging the pure hausmannite (HM) and Co-doped hausmannite (CoH10) in  
440 dry state for three years,  $14.1 \pm 1.9\%$  of manganite appears in agedHM while  $2.6 \pm 0.7\%$   
441 of manganite is observed in agedCoH10. This clearly suggests the transformation of  
442 hausmannite to manganite. It is proposed that the transformation of hausmannite to  
443 manganite involves  $O_2$  and  $H_2O$  according to the following equation (eq. 1):



444 During hausmannite aging in dry state, Mn(II) on the mineral surfaces are  
445 gradually oxidized by  $O_2$  to form  $-Mn=O$  groups. Then these groups react with  
446 physisorbed  $H_2O$ , leading to the formation of  $-Mn=(OH)_2$  groups. Finally  $-Mn=(OH)_2$   
447 groups are transformed to MnOOH, which is thought to be the rate-determining step  
448 (Kirillov et al., 2009).

449 This transformation processes can be affected by many factors. In the present study,  
450 the  $O_2$  and  $H_2O$  concentrations are limited during hausmannite aging, which is stored  
451 in a closed tube. Thus the transformation rate here is much lower than those in air  
452 (Kirillov et al., 2009) and in high relative humidity(Rabiei et al., 2005). However, the  
453 transformation rate of CoH10 is much lower than that of HM at same conditions. This  
454 may be related to the substitution-induced changes in mineral physicochemical  
455 properties, such as chemical composition, particle size and stability of the host mineral.  
456 Although Co-doped hausmannite samples here show the same cubic morphology as  
457 that of pure hausmannite, statistical analyses of TEM determined particle sizes and the  
458 CSDs obtained by XRD show that the Co-doped crystals are larger than those of HM.  
459 The increase in crystal sizes of CoH5 and CoH10 may make them more stable than HM  
460 (Birkner and Navrotsky, 2014; Gillot et al., 2001), since smaller crystallite size is  
461 reported to promote phase transformation (Birkner and Navrotsky, 2012; Birkner and  
462 Navrotsky, 2014). Additionally, doping Co decreases the  $Mn^{3+}$  content, and suppresses  
463 the Jahn-Teller distortion to make the mineral structure more stable than pure one. The  
464 decrease of  $Mn^{3+}$  may also favor the formation of hausmannite rather than MnOOH  
465 phase (Jha et al., 2012). Our results clearly show that, exotic cation substitution have  
466 great impact on the transformation of hausmannite. Conclusively, the enrichment of

467 various TMs in hausmannite may be an important reason for the stability of these  
468 minerals in natural environments.

469

## 470 **5. Conclusions and environmental implications**

471 Natural hausmannite analogs, including Co-substituted hausmannites with Co/Mn  
472 molar ratios of 0.05 and 0.11 were synthesized at ambient conditions. Cobalt ions  
473 existed as  $\text{Co}^{3+}$  and  $\text{Co}^{2+}$ , substituting for  $\text{Mn}^{3+}$  in the octahedral sites, which resulted  
474 in suppression of the Jahn-Teller distortion and a commensurate decrease in the unit-  
475 cell parameter  $c$ . These Co-doped hausmannite samples had decreased Mn AOS and  
476 increased crystal sizes than HM. Acid dissolution experiments confirmed that Co  
477 incorporated into the mineral structures, and made the mineral more stable. Cobalt K-  
478 edge EXAFS analysis demonstrated that dopants occupied the octahedral sites in the  
479 hausmannite structure. Cobalt doping greatly improved the hausmannite stability  
480 during dry aging at room temperature. After three years of aging in a dry state,  $14.1 \pm$   
481  $1.9\%$  of hausmannite in HM was transformed to manganite, while only  $2.6 \pm 0.7\%$  of  
482 hausmannite in CoH10 was transformed to manganite.

483 Based on the excellent adsorption, reducing and oxidizing reactivity towards a  
484 variety of metal pollutants (Antao et al., 2019; Baron et al., 1998; Bordeneuve et al.,  
485 2010; Green et al., 2004; Lefkowitz and Elzinga, 2015; Song et al., 2020), hausmannite  
486 may play an important role in mediating the mobility and fate of metal nutrients and  
487 contaminants in terrestrial environments. The substitution of TM for lattice Mn in the  
488 hausmannite structure may greatly modify the mineral physicochemical properties and  
489 thus their reactivity. Carefully and accurately investigation of the reactivity of these  
490 doped minerals, which are close to their natural analogues, with nutrients and pollutants,  
491 may help us understand and predict the geochemical behaviors of elements of interest  
492 in natural settings and also benefit us from the design and application of environmental-  
493 friendly Mn oxide materials in pollutant control and remediation.

494

## 495 **Acknowledgments**

496 We gratefully acknowledge Dr. Wei Zhao from Northwest A&F University for  
497 providing the FTIR data of manganite. The authors gratefully thank the Key science  
498 and technology projects of Inner Mongolia autonomous region (2019ZD001), the  
499 National Natural Science Foundations of China (Nos.42077015 and 41771267), the  
500 National Key Research and Development Program of China (No. 2016YFD0800403),  
501 and the Fundamental Research Funds for the Central Universities (Grant 103-  
502 510320036) for the financial support.

503

504

## REFERENCES

- 505 Alvarez, M., Rueda, E.H., Sileo, E.E., 2007. Simultaneous incorporation of Mn and Al in the goethite  
506 structure. *Geochimica et Cosmochimica Acta*, 71(4): 1009-1020.
- 507 Alvarez, M., Sileo, E.E., Rueda, E.H., 2008. Structure and reactivity of synthetic Co-substituted goethites.  
508 *American Mineralogist*, 93(4): 584-590.
- 509 Antao, S.M., Cruickshank, L.A., Hazrah, K.S., 2019. Structural Trends and Solid-Solutions Based on the  
510 Crystal Chemistry of Two Hausmannite (Mn<sub>3</sub>O<sub>4</sub>) Samples from the Kalahari Manganese Field.  
511 *Minerals*, 9(6): 343.
- 512 Baron, V., Gutzmer, J., Rundlof, H., Tellgren, R., 1998. The influence of iron substitution on the magnetic  
513 properties of hausmannite, Mn<sup>2+</sup>(Fe,Mn)<sub>(2)</sub>(<sup>3+</sup>)O<sub>4</sub>. *American Mineralogist*, 83(7-8): 786-793.
- 514 Barreto, M.S.C., Elzinga, E.J., Alleoni, L.R.F., 2020. Hausmannite as potential As(V) filter. Macroscopic  
515 and spectroscopic study of As(V) adsorption and desorption by citric acid. *Environmental*  
516 *Pollution*, 262: 114196.
- 517 Birkner, N., Navrotsky, A., 2012. Thermodynamics of manganese oxides: Effects of particle size and  
518 hydration on oxidation-reduction equilibria among hausmannite, bixbyite, and pyrolusite.  
519 *American Mineralogist*, 97(8-9): 1291-1298.
- 520 Birkner, N., Navrotsky, A., 2014. Rapidly reversible redox transformation in nanophase manganese  
521 oxides at room temperature triggered by changes in hydration. *Proceedings of the National*  
522 *Academy of Sciences*, 111(17): 6209-6214.
- 523 Boland, D.D., Collins, R.N., Glover, C.J., David Waite, T., 2013. An in situ quick-EXAFS and redox  
524 potential study of the Fe(II)-catalysed transformation of ferrihydrite. *Colloids and Surfaces A:*  
525 *Physicochemical and Engineering Aspects*, 435: 2-8.
- 526 Bordeneuve, H. et al., 2010. Structural variations and cation distributions in Mn<sub>3-x</sub>Co<sub>x</sub>O<sub>4</sub> (0 ≤ x ≤ 3)  
527 dense ceramics using neutron diffraction data. *Solid State Sciences*, 12(3): 379-386.
- 528 Boucher, B., Buhl, R., Perrin, M., 1971. Propriétés et structure magnétique de Mn<sub>3</sub>O<sub>4</sub>. *Journal of Physics*  
529 *and Chemistry of Solids*, 32(10): 2429-2437.
- 530 Burns, R.G., 1993. Mineralogical applications of crystal field theory. *Cambridge topics in mineral*  
531 *physics and chemistry*. Cambridge university press, New York.
- 532 Chartier, A., D'Arco, P., Dovesi, R., Saunders, V.R., 1999. Ab initio Hartree-Fock investigation of the  
533 structural, electronic, and magnetic properties of Mn<sub>3</sub>O<sub>4</sub>. *Physical Review B*, 60(60).
- 534 Cornell, R.M., Schwertmann, U., 2003. The iron oxides : structure, properties, reactions, occurrences and  
535 uses. Wiley-VCH, Weinheim.

536 Dong, R. et al., 2013. Enhanced supercapacitor performance of Mn<sub>3</sub>O<sub>4</sub> nanocrystals by doping transition-  
537 metal ions. *ACS Applied Material & Interfaces*, 5(19): 9508-16.

538 Feng, X.H., Liu, F., Tan, W.F., Liu, X.W., 2004. Synthesis of birnessite from the oxidation of Mn<sup>2+</sup> by O<sub>2</sub>  
539 in alkali medium: Effects of synthesis conditions. *Clays and Clay Minerals*, 52(2): 240-250.

540 Gillot, B., El Guendouzi, M., Laarj, M., 2001. Particle size effects on the oxidation–reduction behavior  
541 of Mn<sub>3</sub>O<sub>4</sub> hausmannite. *Materials Chemistry and Physics*, 70(1): 54-60.

542 Giovannelli, F. et al., 2012. Synthesis of manganese spinel nanoparticles at room temperature by  
543 coprecipitation. *Journal of Solid State Chemistry*, 192: 109-112.

544 Green, W.J. et al., 2004. Nickel, Copper, Zinc and Cadmium cycling with manganese in Lake Vanda  
545 (Wright Valley, Antarctica). *Aquatic Geochemistry*, 10(3): 303-323.

546 Hao, X. et al., 2011. Mild aqueous synthesis of octahedral Mn<sub>3</sub>O<sub>4</sub> nanocrystals with varied oxidation  
547 states. *Colloids and Surfaces A: Physicochemical and Engineering Aspects*, 374(1-3): 42-47.

548 Hirai, S. et al., 2016. Enhancement of the oxygen evolution reaction in Mn<sup>3+</sup>-based electrocatalysts:  
549 correlation between Jahn–Teller distortion and catalytic activity. *RSC Advances*, 6(3): 2019-  
550 2023.

551 Ilton, E.S., Post, J.E., Heaney, P.J., Ling, F.T., Kerisit, S.N., 2016. XPS determination of Mn oxidation  
552 states in Mn (hydr)oxides. *Applied Surface Science*, 366: 475-485.

553 Jarosch, D., 1987. Crystal structure refinement and reflectance measurements of hausmannite, Mn<sub>3</sub>O<sub>4</sub>.  
554 *Mineralogy & Petrology*, 37(1): 15-23.

555 Jha, A., Thapa, R., Chattopadhyay, K.K., 2012. Structural transformation from Mn<sub>3</sub>O<sub>4</sub> nanorods to  
556 nanoparticles and band gap tuning via Zn doping. *Materials Research Bulletin*, 47(3): 813-819.

557 Johnson, K.L. et al., 2018. Dissolved Mn(III) in water treatment works: Prevalence and significance.  
558 *Water Research*, 140: 181-190.

559 Julien, C.M., Massot, M., Poinignon, C., 2004. Lattice vibrations of manganese oxides: Part I. Periodic  
560 structures. *Spectrochimica Acta Part A: Molecular and Biomolecular Spectroscopy*, 60(3): 689-  
561 700.

562 Kelly, S.D., Hesterberg, D., Ravel, B., 2008. Analysis of soils and minerals using X-ray absorption  
563 spectroscopy. In: Ulrey, A.L., Drees, R.L. (Eds.), *Methods of Soil Analysis, Part 5-  
564 Mineralogical Methods*. Soil Science Society of America.

565 Kim, H. et al., 2012. Multicomponent effects on the crystal structures and electrochemical properties of  
566 spinel-structured M<sub>3</sub>O<sub>4</sub> (M = Fe, Mn, Co) anodes in lithium rechargeable batteries. *Chemistry  
567 of Materials*, 24(4): 720-725.

568 Kim, J.G., Dixon, J.B., Chusuei, C.C., Deng, Y.J., 2002. Oxidation of chromium(III) to (VI) by  
569 manganese oxides. *Soil Science Society of America Journal*, 66(1): 306-315.

570 Kirillov, S.A. et al., 2009. Oxidation of synthetic hausmannite (Mn<sub>3</sub>O<sub>4</sub>) to manganite (MnOOH). *Journal  
571 of Molecular Structure*, 928(1): 89-94.

572 Kohler, T., Armbruster, T., Libowitzky, E., 1997. Hydrogen bonding and Jahn–Teller distortion in  
573 groutite, α-MnOOH, and manganite, γ-MnOOH, and their relations to the manganese dioxides  
574 ramsdellite and pyrolusite. *Journal of Solid State Chemistry*, 133(2): 486-500.

575 Kwon, K.D., Refson, K., Sposito, G., 2009. Zinc surface complexes on birnessite: A density functional  
576 theory study. *Geochimica Et Cosmochimica Acta*, 73(5): 1273-1284.

577 Lan, S. et al., 2017. Mechanisms of Mn(II) catalytic oxidation on ferrihydrite surfaces and the formation  
578 of manganese (oxyhydr)oxides. *Geochimica Et Cosmochimica Acta*, 211: 79-96.

579 Lefkowitz, J.P., Elzinga, E.J., 2015. Impacts of aqueous Mn(II) on the sorption of Zn(II) by hexagonal

580 birnessite. *Environmental Science & Technology*, 49(8): 4886-4893.

581 Lide, D.R., "Mickey" Haynes, W.M., 2010. CRC handbook of chemistry and physics. CRC Press, Florida.

582 Liu, L. et al., 2019. The speciation of Cd in Cd-Fe coprecipitates: Does Cd substitute for Fe in goethite  
583 structure? *ACS Earth and Space Chemistry*, 3(10): 2225-2236.

584 Manceau, A., Silvester, E., Bartoli, C., Lanson, B., Drits Victor, A., 1997. Structural mechanism of Co<sup>2+</sup>  
585 oxidation by the phyllosmanganate buserite, *American Mineralogist*, pp. 1150.

586 McKenzie, R., 1970. The reaction of cobalt with manganese dioxide minerals. *Soil Research*, 8(1): 97-  
587 106.

588 Nogués, M., Poix, P., 1974. Effet Jahn-Teller coopératif dans le système Mn<sub>3</sub>O<sub>4</sub> · Mn<sub>2</sub>SnO<sub>4</sub>. *Journal of*  
589 *Solid State Chemistry*, 9(4): 330-335.

590 Pozas, R., Rojas, T.C., Ocana, M., Serna, C.J., 2004. The nature of Co in synthetic Co-substituted  
591 goethites. *Clays and Clay Minerals*, 52(6): 760-766.

592 Qin, Z. et al., 2017. Local structure of Cu<sup>2+</sup> in Cu-doped hexagonal turbostratic birnessite and Cu<sup>2+</sup>  
593 stability under acid treatment. 466: S0009254117303984.

594 Rabiei, S. et al., 2005. Conversion of hausmanite (Mn<sub>3</sub>O<sub>4</sub>) particles to nano-fibrous manganite (MnOOH)  
595 at ambient conditions. *Journal of Materials Science*, 40(18): 4995-4998.

596 Rajeesh Kumar, N.K., Vasylechko, L., Sharma, S., Yadav, C.S., Selvan, R.K., 2021. Understanding the  
597 relationship between the local crystal structure and the ferrimagnetic ordering of Co<sub>x</sub>Mn<sub>3-x</sub>O<sub>4</sub>  
598 (x = 0–0.5) solid solutions. *Journal of Alloys and Compounds*, 853: 157256.

599 Ravel, B., Newville, M., 2006. ATHENA and ARTEMIS: Interactive graphical data analysis using  
600 IFEFFIT. *Physica Scripta*, 2005(T115): 1007.

601 Rehr, J.J., Albers, R.C., Zabinsky, S.I., 1992. High-order multiple-scattering calculations of x-ray-  
602 absorption fine structure. *Physical Review Letters*, 69(23): 3397-3400.

603 Şahin, B., Aydin, R., Cetin, H., 2020. Tuning the morphological, structural, optical and dielectric  
604 properties of hausmannite (Mn<sub>3</sub>O<sub>4</sub>) films by doping heavy metal lead. *Superlattices and*  
605 *Microstructures*, 143: 106546.

606 Shannon, R., 1976. Revised effective ionic radii and systematic studies of interatomic distances in halides  
607 and chalcogenides. *Acta Crystallographica Section A*, 32(5): 751-767.

608 Shaughnessy, D.A. et al., 2003. Molecular interfacial reactions between Pu(VI) and manganese oxide  
609 minerals manganite and hausmannite. *Environmental Science & Technology*, 37(15): 3367-  
610 3374.

611 Sherman, D.M., 1984. The electronic structures of manganese oxide minerals. *American Mineralogist*,  
612 69(7-8): 788-799.

613 Song, B., Cerkez, E.B., Elzinga, E.J., Kim, B., 2020. Effects of Ni incorporation on the reactivity and  
614 stability of hausmannite (Mn<sub>3</sub>O<sub>4</sub>): Environmental implications for Mn, Ni, and As solubility and  
615 cycling. *Chemical Geology*, 558: 119862.

616 Spencer, C.D., Schroerer, D., 1974. Mössbauer study of several cobalt spinels using Co<sup>57</sup> and Fe<sup>57</sup>.  
617 *Physical Review B*, 9(9): 3658-3665.

618 Sukhdev, A. et al., 2020. Synthesis, phase transformation, and morphology of hausmannite Mn<sub>3</sub>O<sub>4</sub>  
619 nanoparticles: photocatalytic and antibacterial investigations. *Heliyon*, 6(1): e03245.

620 Valldor, M., Andersson, M., 2002. The structure of the new compound YBaCo<sub>4</sub>O<sub>7</sub> with a magnetic feature.  
621 *Solid State Sciences*, 4(7): 923-931.

622 Wilk, P.A., Shaughnessy, D.A., Wilson, R.E., Nitsche, H., 2005. Interfacial interactions between Np(V)  
623 and manganese oxide minerals manganite and hausmannite. *Environmental Science &*

624 Technology, 39(8): 2608-2615.

625 Xu, H., Xu, S., Wang, H., Yan, H., 2005. Characterization of hausmannite  $Mn_3O_4$  thin films by chemical  
626 bath deposition. *Journal of The Electrochemical Society*, 152(12): C803.

627 Yin, H. et al., 2014. Effects of Co and Ni co-doping on the structure and reactivity of hexagonal birnessite.  
628 *Chemical Geology*, 381: 10-20.

629 Yin, H. et al., 2013. Effects of Fe doping on the structures and properties of hexagonal birnessites -  
630 Comparison with Co and Ni doping. *Geochimica Et Cosmochimica Acta*, 117: 1-15.

631 Yin, H. et al., 2011.  $Co^{2+}$ -exchange mechanism of birnessite and its application for the removal of  $Pb^{2+}$   
632 and As(III). *Journal of Hazardous Materials*, 196: 318-326.

633 Yin, H. et al., 2015. High Co-doping promotes the transition of birnessite layer symmetry from  
634 orthogonal to hexagonal. *Chemical Geology*, 410: 12-20.

635 Yin, H. et al., 2020a. Effects of Co(II) ion exchange, Ni(II)- and V(V)-doping on the transformation  
636 behaviors of Cr(III) on hexagonal turbostratic birnessite-water interfaces. *Environmental*  
637 *Pollution*, 256: 113462.

638 Yin, H. et al., 2012. Characterization of Ni-rich hexagonal birnessite and its geochemical effects on  
639 aqueous  $Pb^{2+}/Zn^{2+}$  and As(III). *Geochimica Et Cosmochimica Acta*, 93: 47-62.

640 Yin, H. et al., 2020b. Preference of Co over Al for substitution of Fe in goethite ( $\alpha$ -FeOOH) structure:  
641 Mechanism revealed from EXAFS, XPS, DFT and linear free energy correlation model.  
642 *Chemical Geology*, 532: 119378.

643 Zhang, F., Zhang, X.G., Hao, L., 2011. Solution synthesis and electrochemical capacitance performance  
644 of  $Mn_3O_4$  polyhedral nanocrystals via thermolysis of a hydrogen-bonded polymer. *Materials*  
645 *Chemistry & Physics*, 126(3): 853-858.

646 Zhao, Q., Yan, Z., Chen, C., Chen, J.J.C.R., 2017. Spinel: Controlled preparation, oxygen  
647 reduction/evolution reaction application, and beyond. *Chemical Reviews*, 117(15): 10121.

648 Zhao, Y., Li, C., Li, F., Shi, Z., Feng, S., 2011. One-step synthesis of highly water-dispersible  $Mn_3O_4$   
649 nanocrystals. *Dalton Trans*, 40(3): 583-8.

650

651 **Table 1.** Co K-edge EXAFS structural parameters obtained from the fit of Co-doped  
 652 hausmannites.

Octahedron	CoH5	CoH10
Co-O		
CN <sup>a</sup>	6	6
R (Å) <sup>a</sup>	1.968	1.970(12)
$\sigma^2$ (Å <sup>2</sup> ) <sup>a</sup>	0.0067(12)	0.0072
Co-Mn(Co) <sub>OES<sub>x</sub></sub> <sup>b</sup>		
CN	2	2
R (Å)	2.821(65)	2.798(43)
$\sigma^2$ (Å <sup>2</sup> )	0.0110(63)	0.0113(35)
Co-Mn(Co) <sub>OES<sub>z</sub></sub> <sup>b</sup>		
CN	4	4
R (Å)	3.023(44)	3.005(29)
$\sigma^2$ (Å <sup>2</sup> )	0.0110(63)	0.0113(35)
Co-Mn(Co) <sub>OTCS<sub>x</sub></sub> <sup>b</sup>		
CN	4	4
R (Å)	3.360	3.383(19)
$\sigma^2$ (Å <sup>2</sup> )	0.0068(30)	0.0055(11)
Co-Mn(Co) <sub>OTCS<sub>z</sub>/TT</sub> <sup>b</sup>		
CN	2	2
R (Å)	3.779(24)	3.771(19)
$\sigma^2$ (Å <sup>2</sup> )	0.0011(17)	0.0032(17)
E <sub>0</sub> (eV)	-3.4(33)	-1.9(21)
Chi Sq.	126.39	91.27
R factor	0.0617	0.0233

653 Notes: <sup>a</sup>CN = coordination number; R = interatomic distance;  $\sigma^2$  = Debye–Waller factor;  
 654 E<sub>0</sub> = energy shift; Chi Sq. = chi-squared statistic.

655 <sup>b</sup>OES<sub>x</sub> and OES<sub>z</sub> refer to edge-sharing octahedra in the x- and z-axis; OTCS<sub>x</sub> and  
 656 OTCS<sub>z</sub> refer to octahedron-tetrahedron corner-sharing pairs in the x- and z-axis; TT  
 657 refers to the nearest tetrahedron-tetrahedron pairs.

658

659 **Table 2.** Electron structure, octahedral coordination radius (CR), electronegativity ( $\chi$ ),  
660 ionization potential ( $\eta$ ), crystal field stabilization energy (CFSE), pairing energy (P)  
661 and bond dissociation energy (BDE) of Mn and Co.

Cation		Electronic structure	Configuration	CR (Å) <sup>a</sup>	$\chi^b$	$\eta^c$ (eV)	$\Delta^d$ (kJ/mol)	CFSE <sup>d</sup> (kJ/mol)	P <sup>e</sup> (kJ/mol)	BDE <sup>c</sup> (kJ/mol)
Mn	II	3d <sup>5</sup>	4(LS)	(e) <sup>4</sup> (t <sub>2</sub> ) <sup>1</sup>	—	—	39.8	79.6	285.0	362 ± 25
			4(HS)	(e) <sup>2</sup> (t <sub>2</sub> ) <sup>3</sup>	0.80	1.4934		0		
			6(LS)	(t <sub>2g</sub> ) <sup>5</sup>	0.81	1.4903	89.8	179.6		
			6(HS)	(t <sub>2g</sub> ) <sup>3</sup> (e <sub>g</sub> ) <sup>2</sup>	0.97	1.4407		0		
	III	3d <sup>4</sup>	4(LS)	(e) <sup>4</sup>	—	—	51.2	111.6	301.6	
			4(HS)	(e) <sup>2</sup> (t <sub>2</sub> ) <sup>2</sup>	—	—		67.0		
			6(LS)	(t <sub>2g</sub> ) <sup>4</sup>	0.72	1.7052	251.3	402.1		
			6(HS)	(t <sub>2g</sub> ) <sup>3</sup> (e <sub>g</sub> ) <sup>1</sup>	0.785	1.6753		150.8		
Co	II	3d <sup>7</sup>	4(LS)	(e) <sup>4</sup> (t <sub>2</sub> ) <sup>3</sup>	—	—	48.9	58.7	250	
			4(HS)	(e) <sup>4</sup> (t <sub>2</sub> ) <sup>3</sup>	0.72	1.5882		58.7		
			6(LS)	(t <sub>2g</sub> ) <sup>6</sup> (e <sub>g</sub> ) <sup>1</sup>	0.79	1.5665	110.1	198.2		
			6(HS)	(t <sub>2g</sub> ) <sup>5</sup> (e <sub>g</sub> ) <sup>2</sup>	0.885	1.5371		88.1		
	III	3d <sup>6</sup>	6(LS)	(t <sub>2g</sub> ) <sup>6</sup>	0.685	1.7913	248.4	534.2	282.6	
			6(HS)	(t <sub>2g</sub> ) <sup>4</sup> (e <sub>g</sub> ) <sup>2</sup>	0.75	1.7614		89.0		

662 <sup>a</sup> Data adopted from Shannon (1976). <sup>b</sup> Data calculated according to Portier et al. (1994).

663 <sup>c</sup> Data from Lide and “Mickey” Haynes. (2010).

664 <sup>d</sup> Data from Burns (1993) and Huheey et al. (1993). These data were calculated by neglecting the electron  
665 pairing energies and electron-electron effects for simplification.

666 <sup>e</sup> Data from Huheey et al. (1993). These values are for the free ions and may be 15-30% smaller when  
667 cations are chemically coordinated because of the nephelauxetic effects.

668

669 **Figure Captions**

670 **Fig. 1** (a) Powder XRD patterns of HM and Co-doped hausmannite samples, overlaid  
671 with the best Rietveld structure refinement results based on a hausmannite model (ICSD  
672 76088). (b) Powder XRD patterns of three years aged Co-doped samples, agedHM and  
673 agedCoH10, overlaid with the best calculated patterns by quantitative phase analysis  
674 using a hausmannite model (ICDD 76088) and manganite model (ICSD 84949). Blue  
675 lines are experimental data ( $Y_{\text{obs}}$ ), red lines are calculated patterns ( $Y_{\text{calc}}$ ), and the light  
676 gray lines are the difference patterns (Diff)). The reflections of hausmannite are not  
677 labeled while the main peak for manganite ( $\gamma$ -MnOOH) is indicated by dash line. (c)  
678 Crystal diagram of hausmannite (ICSD 76088).

679 **Fig. 2** Typical TEM images of freshly prepared Co-doped hausmannite samples (a, HM;  
680 b, CoH5; c, CoH10), and 3 years aged samples of (d) agedHM and (g) agedCoH10. (e)  
681 and (i) show the SAED patterns of the areas in the blue rectangles in (d) and (g),  
682 respectively, while (f) and (h) are typical HRTEM images for the area in the blue circle  
683 in the inset at right down of panel (f) and the blue rectangle in panel (g) correspondingly.

684 **Fig. 3** FTIR spectra of freshly prepared and 3 years aged Co-doped hausmannite  
685 samples and a synthesized manganite standard.

686 **Fig. 4** Mn 2p spectra of HM and CoH10 (a), and the corresponding Mn 2p<sub>3/2</sub> spectra (b,  
687 c) with the best fit overlaid (The black open circles represent experimental data, red  
688 lines are the best fit to the data, peaks corresponding to Mn<sup>2+</sup>, Mn<sup>3+</sup> and Mn<sup>4+</sup> are shown  
689 as green dot, dash and solid lines respectively, and the gray solid lines at the bottom are  
690 the difference patterns). (d) Linear combination fitting (red dashed lines) of Co K-edge  
691 XANES spectra of CoH5 and CoH10, using CoSO<sub>4</sub> and CoOOH (Yin, 2015 #50) as  
692 references.

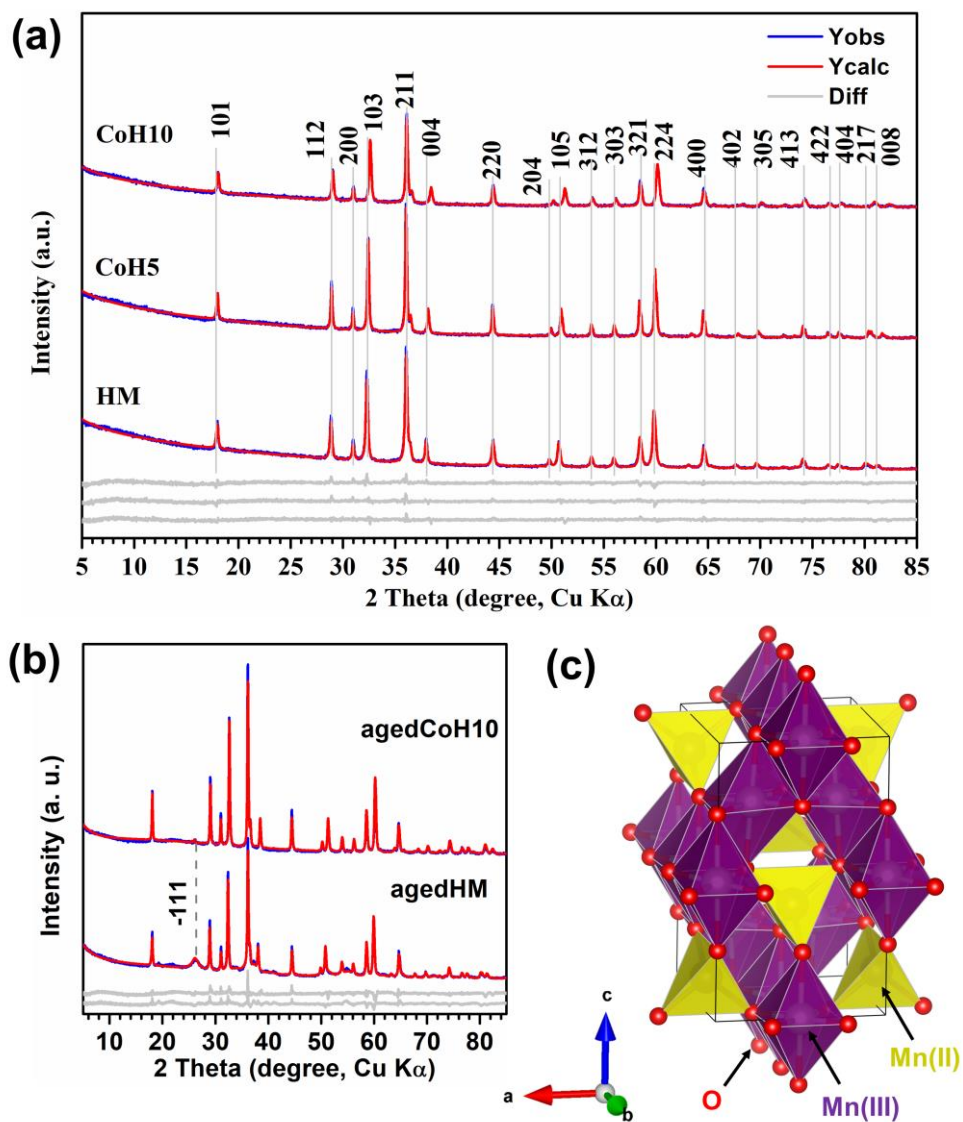
693 **Fig. 5** (a) Mineral dissolution kinetic curves expressed as %Co dissolved ( $\chi_{\text{Co}}$ ) or %Mn  
694 dissolved ( $\chi_{\text{Mn}}$ ) in 2 M HCl solution at 25 °C and (b) the corresponding  $\chi_{\text{Co}}$  versus  $\chi_{\text{Mn}}$   
695 curves of these Co-doped hausmannite samples. In panel a, the inset is the detailed  
696 figure in the first 12 h of the dissolution reactions, the solid lines are the best fit of the  
697 whole dissolution curve with Kabai equation,  $\chi_{\text{Co(Mn)}} = 1 - \exp(-(kt)^\alpha)$ , in which k and  
698  $\alpha$  are constants representing the dissolution rate constant and the characteristics of the

699 mineral structure, and the corresponding fitting parameters are listed in the table  
700 inserted in the panel. In panel b, the red solid line is the 1:1 line.

701 **Fig. 6** Comparison of  $k^3$ -weighted Co K-edge EXAFS (a) and the corresponding  
702 Fourier transformed (FTs) spectra (b) of CoH10 and that of synthesized CoSO<sub>4</sub> and  
703 CoOOH from our previous study (Yin et al., 2015). In panel b, the magnitudes of first  
704 Co-O peaks were normalized. The Co K-edge EXAFS (c) and the corresponding  
705 Fourier transformed (FTs) spectra (d) of CoH5 and CoH10, overlaid with the best fitting  
706 by assuming that all the Co cations occupy the octahedral sites. Blue lines are  
707 experimental data and dashed red lines are the best fits.

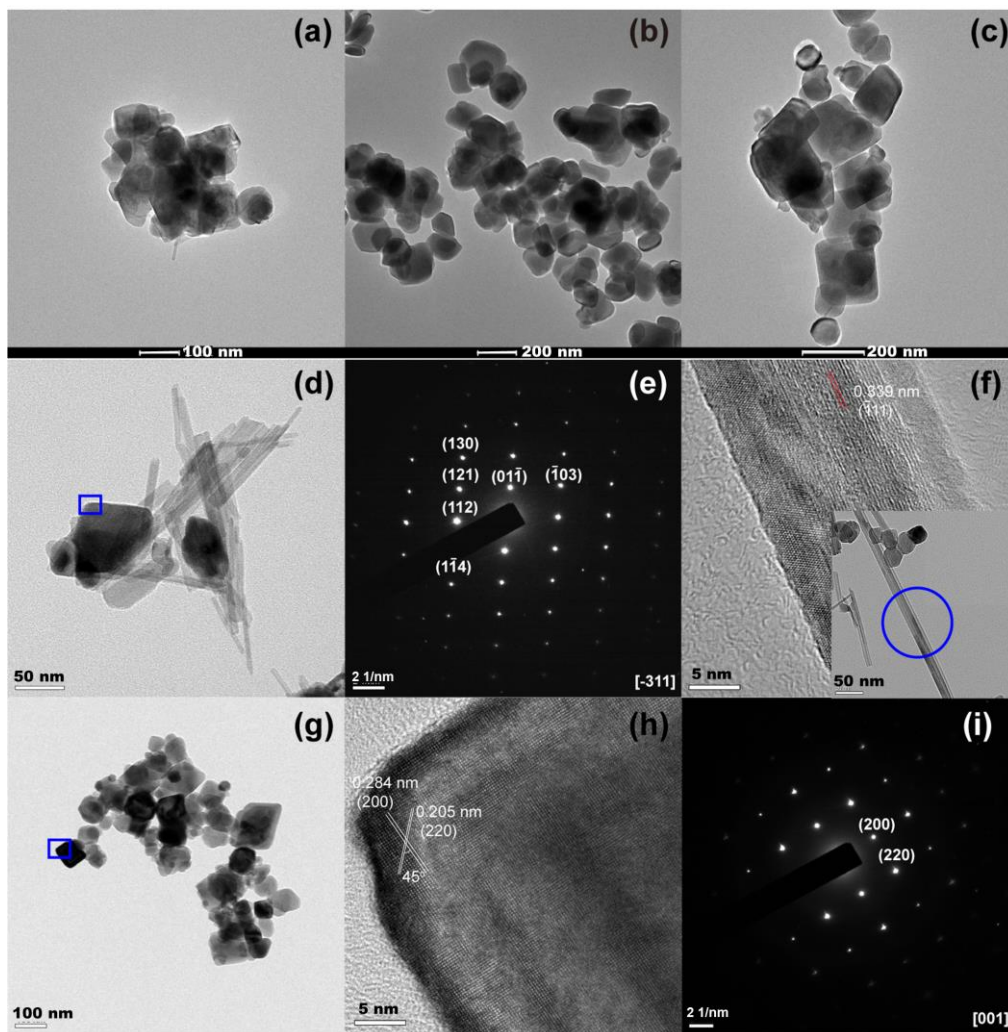
708 **Fig. 7** Comparison of the  $c/\sqrt{2}a$  of the Co-doped hausmannite samples in the present  
709 study with those of the Mn<sub>3-x</sub>Co<sub>x</sub>O<sub>4</sub> nanoparticles from previous studies (Bordeneuve  
710 et al., 2010; Hirai et al., 2016; Rajeesh Kumar et al., 2021). The solid lines represent  
711 the linear fitting of these data with  $x < 1$ .

712



713

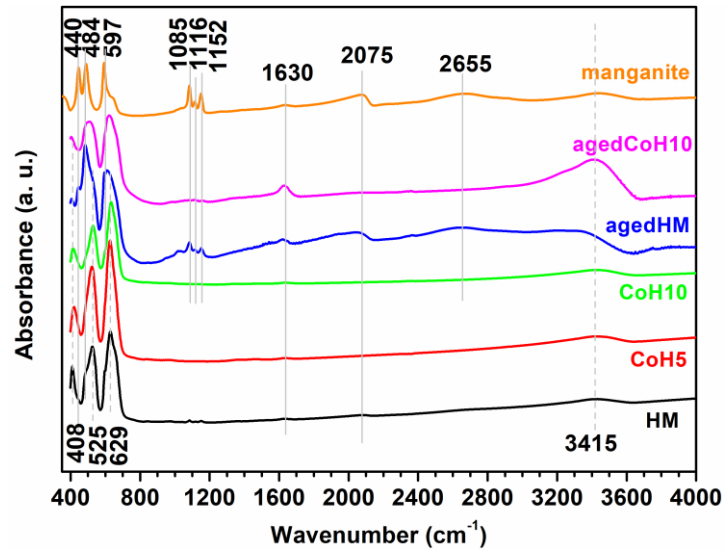
714 Fig. 1



715

716 **Fig. 2**

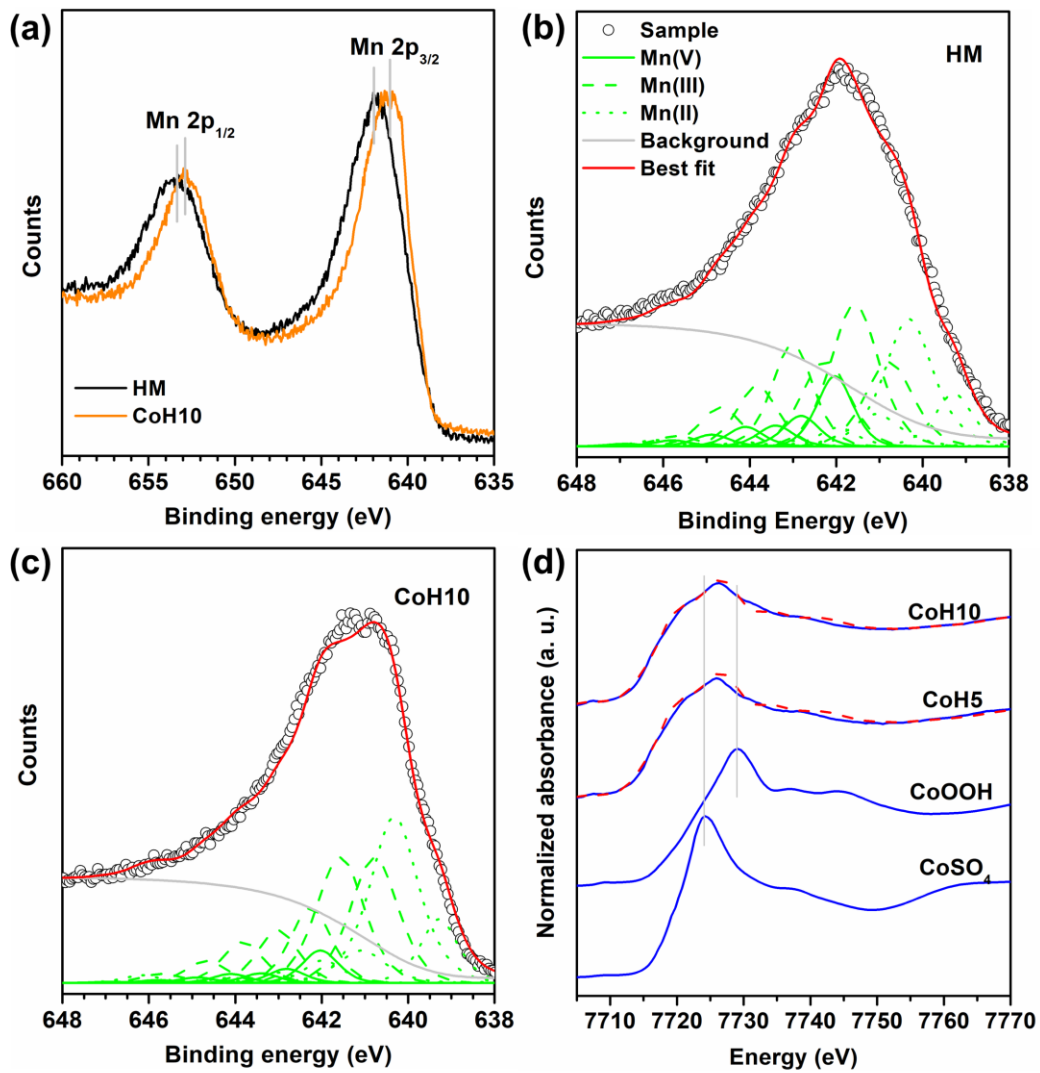
717



718

719 **Fig. 3**

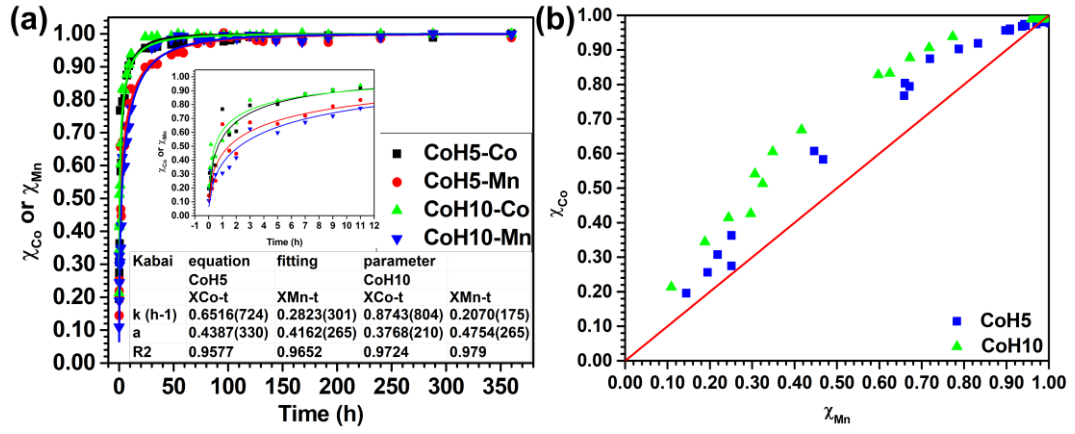
720



721

722 **Fig. 4**

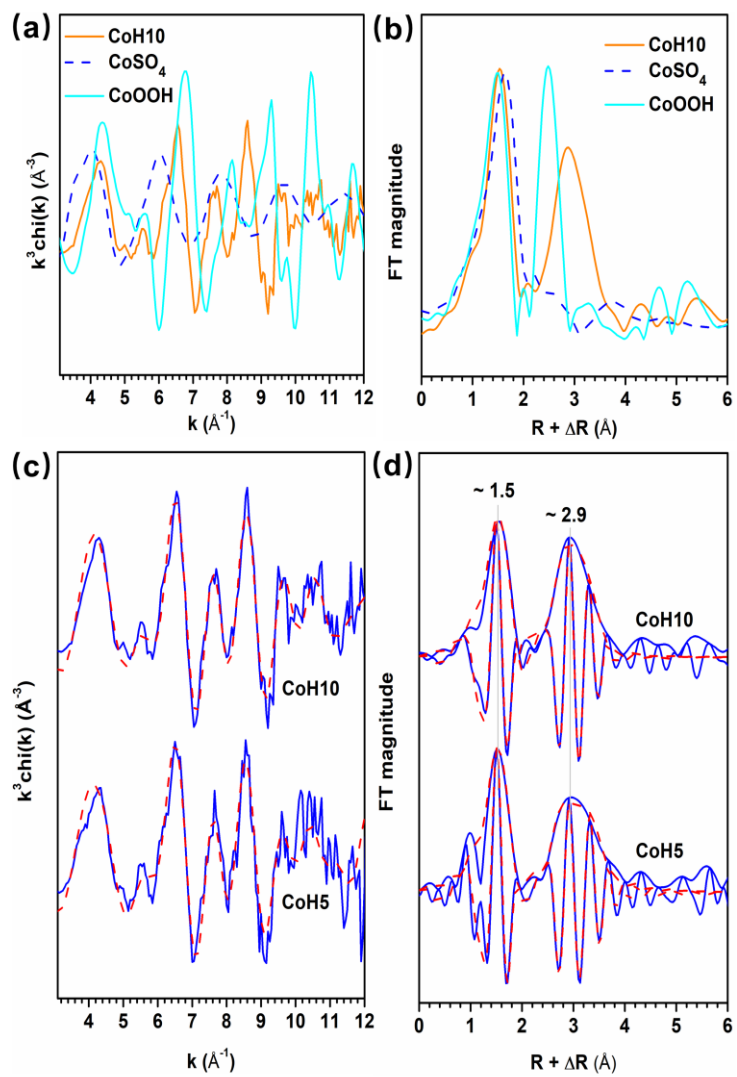
723



724

725 **Fig. 5**

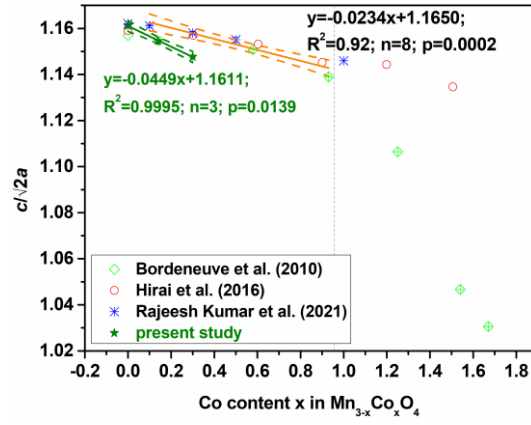
726



727

728 **Fig. 6**

729



730

731 **Fig. 7**